

Boundary layer hydrodynamics of patchy biofilms

Elizabeth A. K. Murphy, Julio M. Barros, Michael P. Schultz, Karen A. Flack, Cecily N. Steppe & Matthew A. Reidenbach

To cite this article: Elizabeth A. K. Murphy, Julio M. Barros, Michael P. Schultz, Karen A. Flack, Cecily N. Steppe & Matthew A. Reidenbach (2022): Boundary layer hydrodynamics of patchy biofilms, *Biofouling*, DOI: [10.1080/08927014.2022.2117033](https://doi.org/10.1080/08927014.2022.2117033)

To link to this article: <https://doi.org/10.1080/08927014.2022.2117033>

 View supplementary material 

 Published online: 05 Sep 2022.

 Submit your article to this journal 

 Article views: 2

 View related articles 

 View Crossmark data 



Boundary layer hydrodynamics of patchy biofilms

Elizabeth A. K. Murphy^{a†} , Julio M. Barros^{b‡} , Michael P. Schultz^c , Karen A. Flack^b, Cecily N. Steppe^d and Matthew A. Reidenbach^a 

^aDepartment of Environmental Sciences, University of Virginia, Charlottesville, USA; ^bDepartment of Mechanical Engineering, United States Naval Academy, Annapolis, Maryland, USA; ^cDepartment of Naval Architecture and Ocean Engineering, United States Naval Academy, Annapolis, Maryland, USA; ^dDepartment of Oceanography, United States Naval Academy, Annapolis, Maryland, USA

ABSTRACT

Algal biofilms, ubiquitous in aquatic systems, reduce the performance of engineered systems and alter ecosystem processes. Biofilm morphology is dynamic throughout community development, with patchiness occurring due to periodic sloughing, but little is known about how community level physical structure affects hydrodynamics. This study uses high resolution particle image velocimetry (PIV) to examine spatially explicit turbulence over sparse, uniform and patchy biofilm at turbulent Reynolds numbers. All biofilms increase the near-bed turbulence production, Reynolds shear stress, and rotational flow compared to a smooth wall, and non-uniform biofilms have the greatest increase in these parameters, compared with a uniform or sparse biofilm. However, a higher drag coefficient over uniform biofilm compared with non-uniform biofilm indicates that percent coverage (the amount of area covered by the biofilm) is a useful predictor of a biofilm's relative effect on the total drag along surfaces, and in particular the effect on ship performance.

ARTICLE HISTORY

Received 26 November 2021
Accepted 19 August 2022

KEYWORDS

Biofouling; algal biofilm;
turbulence; roughness;
boundary layer; PIV

Introduction

Biofilms are aggregates of bacterial and algal cells that form a thin layer on most aquatic surfaces, including natural surfaces such as streambeds and coral reefs, as well as engineered surfaces such as ship hulls and pipes. In habitats such as streams and intertidal mudflats, biofilms are considered ecosystem engineers because they alter nutrient cycling and sediment stability (Decho 2000; Battin et al. 2003). On corals, algal biofilm growth can be detrimental to the reef community, damping flow velocity at the coral surface, inhibiting nutrient exchange, and effectively smothering the coral (Stocking et al. 2016). On Naval and other ocean-going vessels, biofilms dominated by diatoms and bacteria are the most common biofouling community (Hunsucker et al. 2014; Schultz et al. 2015), and substantially increase powering costs by increasing the frictional resistance of the ship surface (Schultz et al. 2011; Hunsucker et al. 2018). In addition to the economic costs associated with biofilm fouling, there is a concomitant increase in greenhouse

gas emissions during shipping and Naval activities (Swain 2010). This increased skin friction due to biofilm fouling can also impact other engineered systems, such as by decreasing the capacity of hydroelectric canals (Andrewartha et al. 2010).

Biofilms are also important to fouling community development, as biofilm fouled surfaces are more likely to be colonized by other fouling organisms than non-biofilm-fouled surfaces (Dobretsov and Rittschof 2020). This can mean that biofilm growth conditions the surface for further attachment of hard fouling organisms, such as barnacles, that have an even greater drag penalty on a ship. Larvae of some fouling species may be induced to settle by hydrodynamic cues related to roughness (Fuchs et al. 2007), or by chemical cues released by the biofilm (Hadfield and Paul 2001). Turbulence is critical to larval settlement, both for delivery of larvae to the bed (Eckman 1990; Hata et al. 2017), as well as by triggering sinking behavior when larvae recognize the hydrodynamic cues of a favorable settlement location (Koehl 2007).

CONTACT Elizabeth A. K. Murphy  eam6vf@virginia.edu

[†]Present address: Department of Zoology, Stockholm University, SE-106 91 Stockholm, Sweden.

[‡]Present address: Fluid Mechanics Unit, Okinawa Institute of Science and Technology, 1919-1 Tancha, Onna-son, Kunigami-gun, Okinawa 904-0495, Japan.

 Supplemental data for this article can be accessed online at <https://doi.org/10.1080/08927014.2022.2117033>.

© This work was authored as part of the Contributor's official duties as an Employee of the United States Government and is therefore a work of the United States Government. In accordance with 17 U.S.C. 105, no copyright protection is available for such works under U.S. Law.

Therefore, the ways in which biofilms alter boundary layer turbulence may be important in regulating the development of the fouling community as a whole.

The physical structure of biofilms is dynamic and governed in large part by local hydrodynamics, especially the wall shear stress (Zargiel and Swain 2014). For example, the species composition and physical structure of biofilms on a ship hull varies along the length, due to changes in the local shear stress (Hunsucker et al. 2014), and stream biofilms grown under varying friction velocities vary in community and physical structure, and in their resistance to sloughing (Graba et al. 2013). During the growth of a biofilm under unidirectional shear, highly flexible, viscoelastic protrusions on the biofilm surface form as chains of diatoms and clump together into macroscopic streamers (Celler et al. 2014). Streamers may serve to streamline the biofilm and reduce hydrodynamic stresses on it, as well as increasing nutrient access by disrupting the diffusive boundary layer (Taherzadeh et al. 2012).

Development of the biofilm community depends on both the initial settlement of microbial cells and subsequent growth of the community, and on the detachment of biofilm, often due to sloughing events (Graba et al. 2014; Van Mooy et al. 2014). Sloughing of the biofilm, a result of shear stress, results in biofilm patchiness (Stoodley et al. 1999), and in some systems such as streams, occurs on a periodic basis (Graba et al. 2014). Ship hulls coated in fouling release paints are designed to facilitate sloughing, which can result in sparse or patchy biofilm fouling as ships are underway (Schultz et al. 2015). Sloughing off and erosion of biofilms can also be a dispersal mechanism for biofilm associated microorganisms (Van Mooy et al. 2014).

Biofilms appear to alter boundary layer hydrodynamics in ways that are similar to rigid roughness (Walker et al. 2013; Murphy et al. 2018). When roughness is added to a surface, the frictional drag is increased along with near-bed turbulent kinetic energy (*tke*) and Reynolds shear stresses (RSS) (Grass 1971; Mignot et al. 2009; Reidenbach et al. 2010). The effect of roughness on a flow depends both on the physical properties of the roughness (such as the spacing and flexibility of roughness elements), as well as the hydrodynamics of the flow (Snyder and Castro 2002). At lower Reynolds numbers, the increase in skin friction as a result of surface roughness is due to the form drag of the roughness elements as well as shear stress in the viscous sublayer. As the Reynolds number increases, the skin friction becomes less dependent on viscous interactions at the surface, and

ultimately the skin friction becomes independent of the Reynolds number of the flow. Once this Reynolds number independence is reached for a given rough surface, the flow is considered to be in the fully rough regime (Flack and Schultz 2014). This phenomenon, well studied over rigid roughness, has also been observed over biofilm fouling that consists of more flexible roughness (Schultz et al. 2015). The overall structure of the mean streamwise velocity (U) profile over uniform biofilm is also similar to that seen over rigid roughness (Murphy et al. 2018).

Momentum extracted from the flow predictably shifts the mean velocity profile within the fluid boundary layer, i.e. the average velocity at a given point in the wall-normal direction is less over a rough wall than over a smooth wall (Krogstad and Antonia 1999). However, in many instances, biofilms create an even larger increase in the momentum deficit and drag than would be expected from rigid roughness, with the drag dependent on the flow speed, percent cover of the biofilm, and biofilm thickness (Hartenberger et al. 2020). This is likely due to the compliance of the biofilm as well as the streamers that form on the biofilm surface (Schultz and Swain 1999; Walker et al. 2013). Additionally, biofilms can increase the strength of turbulent sweeps and ejections, similar to what is seen over other types of aquatic vegetation like seagrass (Hansen and Reidenbach 2012), indicating that in some scenarios, biofilms may enhance vertical transport between the bed and water column. Even over relatively uniform biofilm, turbulence data show a high degree of spatial heterogeneity, with hotspots of *tke* production and dispersive stresses at the bed (Murphy et al. 2018). While previous research offers a baseline understanding of spatially integrated flow dynamics over biofilms, or only examines uniform biofilms (Schultz 2000; Walker et al. 2013; Schultz et al. 2015; Murphy et al. 2018), real-world biofilm fouling is often patchy during development of the fouling community or due to being sloughed off under shear (Stoodley et al. 1998; Schultz 2000; Schultz et al. 2003), and spatially explicit data are needed to understand the mechanisms behind biofilm effects on surface bounded flows. This is because biofilm patchiness is likely to influence local hydrodynamics, leading to feedbacks between biofilm morphology, fluid forces on the biofilm, and additional morphology changes due to sloughing (Telgmann et al. 2004). Because biofilms also provide a base aquatic surface on top of which additional settlement of fouling organisms occurs, patchiness effects on boundary layer hydrodynamics

may have implications for the development of fouling communities due to hydrodynamic or chemical cues (Hadfield and Paul 2001; Koehl 2006; Koehl et al. 2022).

While classic rough wall boundary layers shift the velocity profile in a somewhat predictable way, natural systems often have larger roughness elements, such as gravel or vegetation, which produce a plane mixing layer (or shear layer) near the crest of the roughness elements. This mixing layer results in an S-shaped velocity profile, i.e. the streamwise velocity has an inflection point in the near-bed region called the roughness sublayer (Mignot et al. 2009). Above the roughness sublayer, canopy flows exhibit a logarithmic layer, which is used in the determination of the friction velocity (Mignot et al. 2009). In a mixing layer, the Reynolds shear stress (RSS) also peaks in the shear layer near the top of the canopy or roughness elements (Raupach et al. 1996), and turbulence production is also enhanced in the shear layer as well as in the wake region behind vegetation or roughness elements (Raupach and Shaw 1982). Canopy-type flows alter the hydrodynamics of a system and can also have implications for transport of solutes or particles, and it is unknown if patchy biofilms can set up a similar type of flow pattern.

Due to the importance of biofilm boundary layer hydrodynamics to ship performance, as well as biofouling community structure and ecological processes, we compare spatially explicit turbulence structure over patchy biofilm with previously reported measurements over a uniform biofilm and a smooth wall. Here, biofilms were grown under dynamic conditions to achieve a more realistic morphology than biofilm grown under stagnant or slow flow conditions. Particle Image Velocimetry (PIV) was then used to examine the boundary layer over biofilm fouled plates in turbulent flow. The current study builds off of the results presented in Murphy et al. (2018), where the boundary layer over a uniform biofilm under turbulent flow was compared to that over a smooth wall. Detailed flow field analysis is presented of the turbulent boundary layer over patchy biofilms at moderate Reynolds number. Both the spatially integrated hydrodynamics, such as skin friction, as well as spatially discrete hydrodynamics such as the response of local velocity profiles to biofilm topography, are investigated. Analysis of the turbulence structure and the mean velocity profile was guided by the following questions:

1. How does the drag coefficient on a biofilm fouled surface depend on biofilm morphology?

2. What is the local variability of bed shear stress and turbulence over non-uniform biofilms?
3. Does patchiness alter how biofilms impact coherent turbulent motions in wall bounded flow?

Materials and methods

Biofilms

Biofilms were grown from a culture of four genera of diatoms (*Amphora*, *Achnanthes*, *Entomoneis* and *Navicula* spp.) collected from fouled plates exposed in the Indian River Lagoon, FL. These diatoms commonly make up slime fouling on ship hulls and other surfaces (Zargiel et al. 2011; Schultz et al. 2015). Brackish (18 ppt) diatom cultures were maintained in a dynamic slime exposure facility at the United States Naval Academy (USNA). The dynamic slime exposure facility, described in detail in Schultz et al. 2015 is a 450 gallon tank with large (0.20 m x 1.52 m) acrylic plates screwed onto a frame attached to a 61 cm diameter rotating drum (60 rpm; peripheral velocity 1.9 m s^{-1}), so that the plates were fully submerged during rotation. This allowed the biofilm fouling on the plates to occur under shear stress. Because of the length of the plates, rotation occurred in the spanwise direction, meaning that the shear stress was perpendicular to the streamwise direction. Due to the nature of the biofilm growth facility, the shear stress acting on the biofilm as it grows was not measured, however, the peripheral velocity of the biofilm plates is comparable to the freestream velocity (U_e) in the flow tunnel during testing (1.3 m s^{-1}). For this study, it seems reasonable to have differences between the flow conditions under which the biofilms were grown and under which they were tested, because biofilms are often found in variable flow environments. For example, ships may be in port for long periods under tidally-driven flows, and streams and rivers exhibit seasonal changes in hydrology.

Biofilms were grown under grow lights on an 18-hour light, 6-hour dark cycle and were fed once weekly with a modified Guillard's F/2 fertilizer with silicate (Florida Aqua Farms, FL), a standard fertilizer used in aquaculture. The four fouled plates used in this study were exposed to the biofilm culture for approximately 10 weeks. All plates had thick (approximately 1.7 mm), uniform biofilm fouling (Figure 1A), with streamers on the order of 1 mm in length, after the 10-week exposure. Patchy (Figure 1B) and sparse (Figure 1C and D) biofilm fouling was achieved by spraying 3 of the fouled plates with a hose and

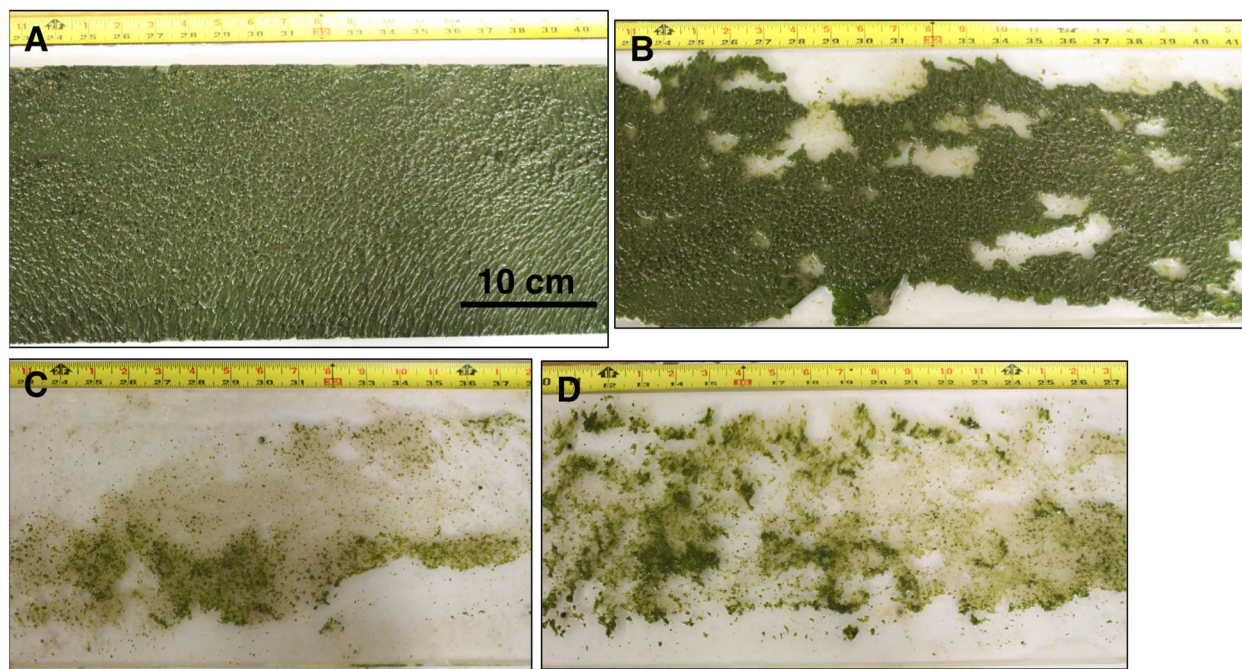


Figure 1. Representative subsection of (A) the uniform biofilm plate (UB); (B) the patchy biofilm (PB-1 and PB-2); (C) sparse biofilm plate SB-1; (D) sparse biofilm plate SB-2.

allowing the biofilm to naturally slough off. Particle Image Velocimetry (PIV) was used to quantify the 2-dimensional flow over three fouled plates, one plate with patchy and two with sparse biofilm coverage. These data are compared to data from a uniformly fouled plate and a smooth plate that was previously published (Murphy et al. 2018). The flow field over the patchy plate was quantified, using PIV, at two different locations in the spanwise direction but the same streamwise location, in order to quantify the semi-local variability of the flow structure. Therefore, a total of 5 biofilm flow fields are compared here: two flow fields over two different sparse biofilm plates, two flow fields over one patchy biofilm plate, and one over a uniform biofilm, taken from Murphy et al. 2018. The percent cover and biofilm thickness were determined by measuring the thickness of wet, but air-exposed, biofilm using a wet film thickness paint gage (Model #WF-S; Paul N. Gardner Co., Inc., Pompano Beach, FL, USA). This is a standard method for measuring the thickness of paint and other organic coatings and is readable to ± 13 microns. Biofilm thickness was measured at 33 locations (3 across the plate and 11 along the plate) in a grid with measurements taken every 5 cm in the spanwise direction and every 13 cm in the lengthwise direction, starting 13 cm from the downstream edge, on each biofilm surface (Schultz et al. 2015). Presence/absence of biofilm at each thickness measurement location was used to estimate the percent cover. Note that a

thickness measurement was only taken if biofilm was present. The peak-to-trough distances were measured using a photograph taken by the camera used for PIV while the biofilm was submerged and exposed to the same moderate Reynolds number test flow as during PIV measurements. The high and low points of each peak and trough of the biofilm in the image was selected by hand, and the vertical distance between adjacent peaks and troughs was calculated. The images used to quantify the biofilm topography (one image per set of PIV measurement) had between 76 and 83 pixels per mm, and this allowed for determination of sub-millimeter scale biofilm topography. The mean and maximum peak-to-trough distances are a local measurement of the biofilm roughness measured under flow conditions, giving a better estimate of the roughness acting on the flow. The patchy plate had 88% biofilm coverage, and the two sparse plates had 55% coverage and 85% coverage. The thickness of the patchy and uniform biofilm were both 1.7 mm, because the sloughing simply removed chunks of biofilm, whereas the thickness of the sparse biofilms was less (0.2 and 0.6 mm). The sparse *vs* patchy biofilm distinction is arbitrary, as biofilm characteristics are a continuum, and was based on the mean thickness of the biofilm. The local roughness values were higher for the patchy biofilm (mean peak-to-trough distance of 0.9 and 0.7 mm) than the uniform biofilm (mean peak-to-trough distance 0.5 mm) and the sparse biofilm (mean peak-to-trough distance of 0.3 and

Table 1. Biofilm characteristics and PIV parameters.

	Biofilm thickness Mean (mm)	Biofilm coverage (%)	Mean peak-to- trough dist. (mm)	Max peak-to- trough dist. (mm)	Velocity vector spatial resolution (μm)	Field-of-view size width (mm) \times height (mm)
Smooth wall (SW)	–	–	–	–	144	78.2×51.5
Sparse biofilm 1 (SB-1)	0.2	55	0.3	0.4	191	78.0×52.1
Sparse biofilm 2 (SB-2)	0.6	85	0.8	2.3	210	85.8×57.3
Patchy biofilm 1 (PB-1)	1.7	88	0.9	2.0	205	83.7×53.6
Patchy biofilm 2 (PB-2)	1.7	88	0.7	1.4	201	82.1×51.2
Uniform biofilm (UB)	1.7	100	0.5	0.9	176	72.2×42.0

0.8 mm for the two sparse plates). Biofilm characteristics are summarized in [Table 1](#).

Particle image velocimetry

Velocity measurements were made in a recirculating tunnel facility housed in the US Naval Academy Hydromechanics Laboratory (Volino et al. 2007; Womack et al. 2022). The removeable test plates, on which the biofilm is grown, were placed in the flow tunnel and formed the bottom wall of the test section. The top wall is height adjustable along the length of the test section and allowed for zero pressure gradient flow. The test section is nominally 0.1 m in depth and 0.2 m across, and 2.0 m long. Water was pumped through flow conditioning devices (consisting of a diffuser, honeycomb, mesh screens and a three-dimensional contraction) prior to entering the test section, such that the free-stream turbulence in the test section was less than 0.5% (Volino et al. 2007), where the free-stream turbulence is quantified as the ratio of the root-mean-square velocity (u_{rms}) to the free-stream velocity (U_e).

High resolution particle image velocimetry (PIV) was used to make detailed measurements of the flow in the streamwise-wall-normal ($x - y$) plane over biofilm fouled acrylic plates in the recirculating turbulent tunnel facility. A commercial 2-D PIV system was used, consisting of a 29-megapixel CCD camera (TSI, Shoreview, MN, USA) coupled to a double pulse laser (Quantel). The PIV system and post-processing (performed using Insight 4G version 11, TSI) are described in detail in Volino et al. (2007) and Murphy et al. (2018). 2-D PIV is a standard flow measurement technique wherein the flow was seeded with small, reflective, neutrally buoyant particles (here, $2 \mu\text{m}$ silver coated glass spheres) and illuminated by a thin plane of laser light. Particles were illuminated in successive image pairs, taken $250 \mu\text{s}$ apart, and a recursive cross-correlation technique was used to find the velocity vectors based on statistically likely particle movement between the two frames in successively smaller interrogation windows. The final pass

was 32^2 pixels with 50% overlap, satisfying the Nyquist sampling criterion. The field of view and grid resolution of the velocity fields are given in [Table 1](#). The combination of the high-resolution camera and small window size at the final pass of PIV processing allowed us to achieve high spatial resolution velocity measurements throughout the boundary layer. The low reflectance of the biofilm permitted good PIV data even very near the bed, and care was taken to minimize optical obstruction. Flapping streamers were masked out of the analysis field during processing, so flow immediately around streamers (which were on the order of 1 – 2 mm in length) was not included in our analysis.

Each time-averaged velocity field was composed of 4000 statistically independent velocity fields. Statistical independence of each instantaneous velocity field was ensured by using a low (1 Hz) sampling frequency. Smooth wall data from Murphy et al. (2018) are also presented for comparison. These data were taken over a non-fouled acrylic plate in the same facility as the biofilm data, using the same PIV system described above. The smooth wall PIV data was taken under very similar hydraulic conditions to the biofilm data ([Table 1](#)). This data was taken prior to the biofilm sampling campaign and is also reported in Murphy et al. (2018).

The freestream velocity (U_e), taken as the value of the time-averaged streamwise velocity, U , at the wall-normal distance, y , where $dU/dy \approx 0$, was 1.3 m s^{-1} for all tests (1.1 m s^{-1} for the previously reported uniform biofilm test plate). The boundary layer thickness (δ ; calculated by finding the point where $U = 0.99U_e$) was between 24.5 and 33.8 mm, depending on the biofilm. Flow parameters for each biofilm as well as the smooth wall tests are given in [Table 2](#). All measurements were taken $\sim 1.22 \text{ m}$ downstream of the boundary layer trip (1.1 m from the upstream edge of the fouled plate). Given $\delta = 33.8 \text{ mm}$ for the thickest boundary layer in our tests, and assuming that a rough wall boundary layer is fully developed 20δ from the onset of the roughness (Antonia and Luxton 1971), the measurement location should ensure adequate development of the turbulent boundary layer.

Table 2. Flow parameters of the biofilm-fouled plates, including the uniform biofilm and smooth wall data from Murphy et al. (2018).

	U_e (m s ⁻¹)	δ (mm)	$Re_\tau = \delta^+ = \frac{\delta U_\tau}{\nu} \times 10^3$	U_τ (m s ⁻¹) CSS	U_τ (m s ⁻¹) total stress	ΔU^+	k_s^+	k_s (mm)	$C_f \times 10^{-3}$	ε (mm)
Smooth wall (SW)	1.3	33.6	1.5	0.042	0.041	–	–	–	2.3	0
Sparse biofilm 1 (SB-1)	1.3	25	1.4	0.050	0.049	0.3	5*	0.1*	3.1	0.1
Sparse biofilm 2 (SB-2)	1.3	24.5	1.8	0.067	0.071	7.0	74*	1.0*	5.5	0.8
Patchy biofilm 1 (PB-1)	1.3	33.8	2.8	0.078	0.077	11.3	438	5.2	7.0	0.9
Patchy biofilm 2 (PB-2)	1.3	33.8	2.8	0.079	0.077	10.6	322	3.8	7.0	1.1
Uniform biofilm (UB)	1.1	28.2	2.2	0.071	0.070	11.8	539	6.9	7.9	1.3

δ^+ is the friction Reynold number. *Indicates that these surfaces are likely not in the fully-rough regime, and therefore values for k_s may not be valid.

Averaging approach

Well above the bed, a fully developed rough wall boundary layer is spatially homogenous. However, near the bed this is no longer the case. The roughness sublayer is the thin layer of fluid encompassing the roughness elements and a small amount of fluid above them, where the temporally averaged flow exhibits spatial heterogeneity due to the roughness. The roughness sublayer typically extends to between about 1.5 to 2 or even 5 times the height of the roughness elements (Raupach et al. 1996; Flack et al. 2007; Florens et al. 2013). This study leveraged the high spatial resolution (176 to 210 μm in the streamwise direction; Table 1) of the PIV measurements and used spatial and temporal averaging to examine the turbulence structure of the flow both locally and as integrated over the streamwise length of the PIV window, which ranged from 72.2 mm to 85.8 mm (Raupach and Shaw 1982; Pokrajac et al. 2007; Martino et al. 2012; Kevin et al. 2017). First, each discrete velocity measurement (here either the streamwise (u) or wall-normal (v) component) is averaged over the 4000 time points sampled. Just as Reynolds decomposition separates instantaneous velocity measurements into mean (U) and fluctuating (u') components, a time-averaged flow quantity can be decomposed into its time-and-space-averaged (or double-averaged) and spatially fluctuating ($\sim u$) components (Mignot et al. 2009). For the spatial average, the intrinsic average is used, where the summed velocities at a given height above the bed are divided by the area occupied by the fluid at that height, omitting the area occupied by the roughness elements (Nikora et al. 2007). In the following, an overbar is used to denote time averaging, and angled brackets are used to denote spatial averaging.

Friction velocity determination

In the log-law region of the boundary layer over a rough surface, the velocity profile in inner units (where the terms are normalized by the friction

velocity, U_τ , or the ratio of the kinematic viscosity to the friction velocity, $\frac{\nu}{U_\tau}$) is described in the log-law form by

$$U^+ \equiv \frac{U}{U_\tau} = \frac{1}{\kappa} \ln(y + \varepsilon)^+ + C - \Delta U^+ \quad (1)$$

where U is the mean (time-averaged or double-averaged) streamwise velocity, ε is the wall datum offset (here normalized by the inner units $\frac{\nu}{U_\tau}$, as is y) and ΔU^+ is the roughness function. Both C (the smooth-wall log-law intercept) and κ (the von Kármán constant) are empirically derived universal constants, here set to 5 and 0.41, respectively. The friction velocity, which is directly related to the bed shear stress (τ_w), is an important parameter when considering the effects of roughness on a turbulent boundary layer, but it is notoriously tricky to accurately determine from velocity profiles for rough walls due to the three unknown variables in Equation 1 (U_τ , ε and ΔU^+). Both local and integrated friction velocities were calculated for each biofilm. The local friction velocity (i.e. the friction velocity over a very small streamwise distance—the width of the final pass PIV interrogation window) was calculated using a velocity profile at a discrete streamwise location, and the integrated friction velocity was calculated using the double-averaged velocity, and better represents the overall friction velocity of the surface. To calculate the integrated friction velocity, U_τ , for the biofilm boundary layers, as well as ε and ΔU^+ , the double-averaged velocity profile was analyzed using a relatively new method, comprehensive shear stress analysis (CSS), devised by Womack et al. (2019). Briefly, this method uses an iterative procedure to fit the measured mean streamwise velocity profile and RSS profile to two sets of equations. First, U_τ is estimated by fitting the RSS profile to an extended momentum balance equation (Volino and Schultz 2018) in the region $0.15 < \frac{y-\varepsilon}{\delta-\varepsilon} < 0.30$. Then, using the estimated U_τ , ε and ΔU^+ are found by fitting the mean streamwise velocity in the log-law region ($0.07 < \frac{y-\varepsilon}{\delta-\varepsilon} < 0.15$) to Equation 1. This process is repeated until the three unknown terms converge. The origin of the y axis is initially set

at the maximum height of the biofilm, and is then shifted downward with the addition of the ε term. The local friction velocities were also calculated by applying the CSS method to local velocity profiles. In the following analysis, biofilm shear velocities are compared with smooth wall shear velocity. The shear velocity for the smooth wall used in this comparison is from the PIV data, and was calculated using the CSS method. To further validate the values of U_τ used here, U_τ is additionally calculated from the double-averaged streamwise velocity and RSS profiles, using the total stress method, where $U_\tau = \sqrt{\nu \frac{\partial U}{\partial y} - \langle \overline{u'v'} \rangle}$ at the plateau of the RSS profile in the overlap region of the boundary layer (Schultz and Flack 2007). These results, presented in Table 2, show excellent agreement with the values of U_τ calculated from the CSS method. Because the total stress method often under-estimates values of U_τ , this agreement may mean that our results here underestimate U_τ .

Results and discussion

Velocity and turbulence structure

Previous work has shown that flow over a fairly uniform biofilm exhibits classic log-law behavior (Murphy et al. 2018). Visual inspection of local U and RSS ($\text{RSS} = -\overline{u'v'}$) profiles suggest that patchy biofilms can create localized plane mixing layers, similar to what is seen behind gravel or cobbles. Figure 2 presents selected local streamwise velocity profiles (U) and local RSS profiles, both normalized in outer units, over the biofilms, chosen to highlight the flow shape over different topographical features (peaks, troughs, and plateaus). While the sparse biofilms studied here also show standard log-law behavior, the patchy biofilms appear to create a mixing layer effect downstream of prominent clumps of biofilm (regions of abrupt local changes in biofilm topography in the streamwise direction). Local RSS profiles over the patchy biofilms also show a peak in RSS due to high shear (dU/dy) near the top of the biofilm clumps, which is also indicative of a plane mixing layer (Raupach et al. 1996). While there is some pressure-driven recirculation in the wake of biofilm clumps, in this high submergence scenario ($H-h \gg h$ where H is the height of the flow tunnel (100 mm) and h is the maximum height of a biofilm roughness element (2.3 mm) turbulent stress is likely to dominate. While the overall pressure gradient in the flow tunnel was zero, an estimate of the relative contributions of turbulent stress and pressure driven

flow in the wake region immediately downstream of a roughness element can be calculated. Given that the turbulent stress gradient below the crest of the (Womack et al., 2019) roughness elements is linear, i.e. $\frac{\partial \overline{u'v'}}{\partial y} \sim \frac{\overline{u'v'}|_h}{h}$, and above the roughness elements, $\overline{u'v'}|_h = g \frac{\partial H}{\partial x} (H-h)$, where g is the acceleration due to gravity, the local ratio of turbulent stress to pressure driven flow can be estimated as the following (Nepf and Vivoni 2000; Reidenbach et al. 2010):

$$\frac{\text{turbulent stress}}{\text{pressure}} = \frac{\partial \overline{u'v'} / \partial y}{g \partial H / \partial x} \sim \frac{H}{h} - 1 \quad (2)$$

For the maximum peak-to-trough distance of our patchy biofilm, the turbulent stress to pressure ratio is $100/2.3 - 1 = 43$, suggesting that pressure-driven flow dynamics play only a small role around the biofilm.

It is worth noting that even though the local biofilm topography for the uniform coverage case (Figure 2A) is quite complex, the overall mean velocity and RSS profile behavior is strikingly more homogeneous than the patchy (PB-1 & PB-2) and SB-1 cases (Figure 2B, C and E), which are highly variable in the inner and overlap regions. The *tke*, not shown, similarly exhibits high spatial variability in the inner and overlap regions, with a similar spatial pattern to the RSS. The spatial variability of RSS (and *tke*), is most pronounced over the patchy biofilms and SB-2 biofilm. These results also show that the RSS is elevated over all of the biofilms compared with the sparsest (SB-1), when normalized by the freestream velocity.

The near-bed regions of the labeled velocity profiles are plotted in Figure 2E to highlight the shape of the inversion of the streamwise velocity. The streamwise velocity and RSS behavior over the patchy biofilms is similar to what is seen in canopy flows (Raupach et al. 1996) and behind large protuberances in a gravel bed (Mignot et al. 2009; Reidenbach et al. 2010). These S-shaped velocity profiles indicate areas where there are large, localized contributions to *tke* fluxes, production, and dissipation (Mignot et al. 2009), likely meaning that biofilm patchiness has an outsized effect on boundary layer turbulence. The penetration depth of vortices below the crest height of the biofilm roughness (but not within the biofilm matrix itself, as visual access to flow was lacked) was calculated, measured as the depth where the local turbulent stress declines to 10% of its maximum value (Nepf and Vivoni 2000). All biofilms showed momentum exchange all the way to the bed in locations where the bed is exposed and free of biofilm, or to the lowest point of the biofilm

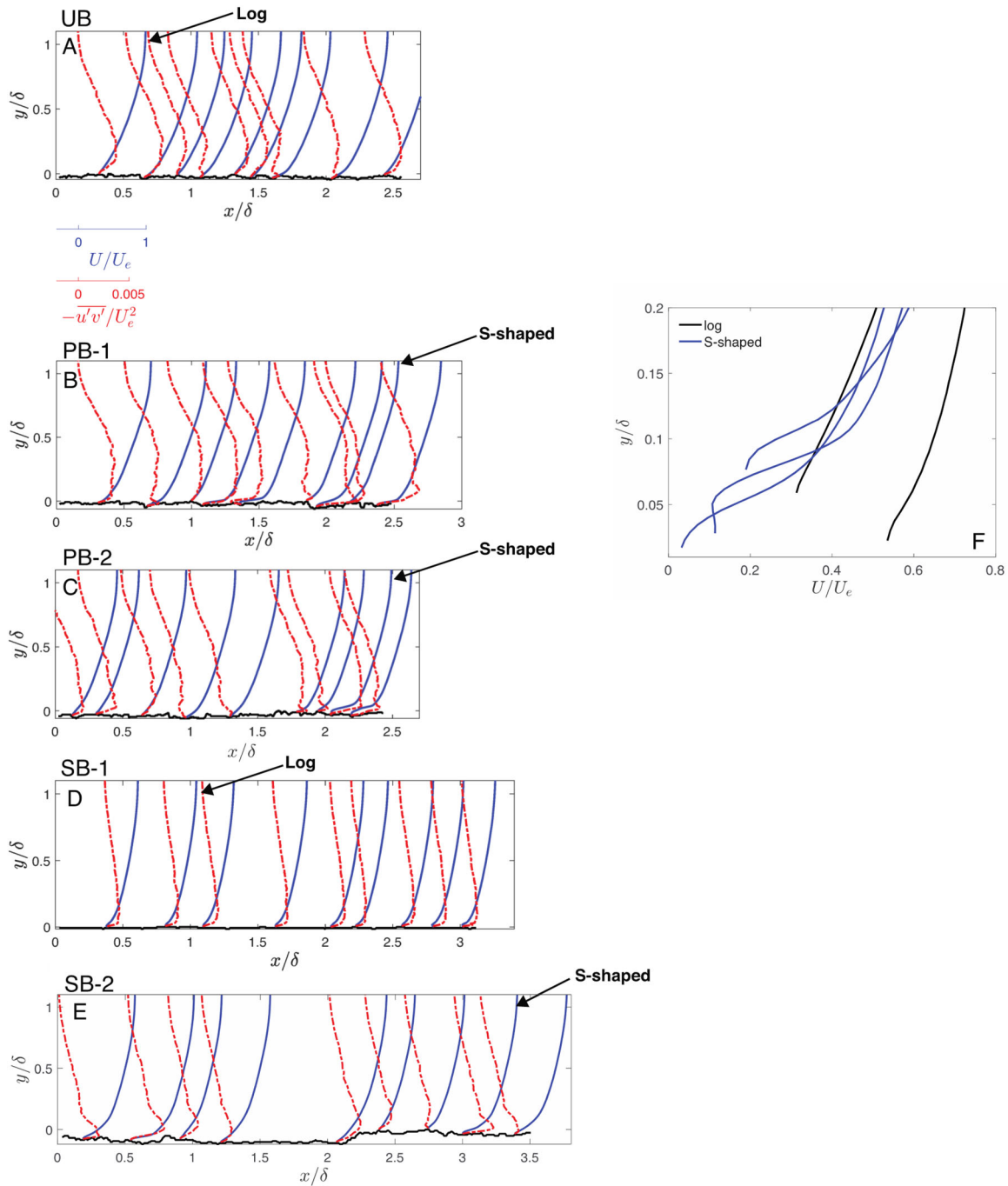


Figure 2. To illustrate the two different shapes of the streamwise velocity ($\frac{U}{U_e}$) and Reynolds shear stress profiles ($RSS = \frac{-u'v'}{U_e^2}$) seen over the biofilms, selected local velocity profiles (blue solid lines) and RSS profiles (red dashed lines) are shown. The profiles are plotted with the vertical distance over the bed on the y-axis (normalized by the boundary layer thickness, δ). To illustrate how the shape of the velocity and RSS profiles changes with location over the biofilm, the solid black line shows the biofilm topography and each profile is shifted along the x-axis. Therefore, each profile has its own origin point, and the base of each profile is anchored to the x axis location at which it was taken. However, the distance from the origin of each profile that corresponds to a given $\frac{U}{U_e}$ or $\frac{-u'v'}{U_e^2}$ value remains the same for each profile and is consistent across all plots, and is shown in the scale bars under panel A. Selected velocity profiles that demonstrate log-like behavior and S-shaped behavior are marked, and the near-bed regions of these profiles are shown in panel E. Panel E depicts a compilation of $\frac{U}{U_e}$ profiles from different biofilm surfaces, therefore the height of the biofilm is not the same for every profile. However, the profiles all start directly at the biofilm, so the height of the biofilm at the location of the profile is at the base of the profile. Note that for better comparison with existing literature on mixing layers, units here have been normalized in outer units.

surface where the bed is covered. This indicates that vertical momentum transport dominates over pressure-driven wake flows behind biofilm clumps. Where the biofilm covers the bed, measuring the water velocity within the biofilm layer was not possible. However, previous research shows that algal biofilms (which have a higher permeability than solely bacterial biofilms) behave like a porous media, with low velocity, pressure-driven flow in the channels within the biofilm matrix (de Beer and Kühn 2001; Depetris et al. 2022). Therefore, sloughing of the biofilm to create greater patchiness may be especially consequential for vertical turbulent transport of nutrients and metabolites to and from lower layers of the biofilm.

Roughness effects

In the few studies that have addressed the effects of biofilms on, e.g. ship performance or hydroelectric canal efficiency, biofilms are considered as added roughness to the surface (Schultz and Swain 1999; Schultz 2000; Andrewartha et al. 2010; Walker et al. 2013; 2014; Hunsucker et al. 2016). This is because, from an engineered systems perspective, the most important consequence of the biofilm fouling is its effect on the surface drag of an object.

Our results show that, hydrodynamically, biofilms add roughness to the surface, resulting in a downward shift of the streamwise velocity profile compared with flow over a smooth wall (Figure 3A) for all tests, though it is minimal for the sparse biofilm plate SB-1. This sparse plate had low coverage, low biofilm thickness, and flow data was taken in an area with low local biofilm roughness (Table 1; Figure 1C). Previous work has shown that biofilm roughness effects depend on both biofilm thickness and coverage, and at the moderate Reynolds number flow used in the current study, the sparse biofilm test cases are likely to be in the transitionally rough regime, as seen for low percent-coverage biofilms in Schultz et al. (2015). Note that the data here are plotted with the vertical dimension (y) on the horizontal axis, and normalized using inner units, for better comparison with other rough wall analyses. The origin of the y axis for each profile is determined by the wall datum offset, ε , values of which are given in Table 2. The values of ε calculated for each biofilm result in a y axis origin located between the bed and the top of the biofilm. For all except the uniform biofilm, the best fit result for ε gives a y axis origin in between the peaks and troughs of the surface of the biofilm. For the uniform biofilm, the best solution gives a value below the surface of

the biofilm, but above the bed. This is physically reasonable as the biofilm is permeable. As noted in Womack et al. (2019), U_τ and ΔU^+ calculated using the CSS method do not show strong dependence on the wall datum offset value, nor on the range of the profile used to fit the log-law.

Plotted in velocity defect form (Figure 3B), reasonably good collapse of the mean velocity profiles is shown. This lack of perfect collapse may indicate that there is some competition between the smooth and rough regions evident in the mean velocity profile averaged over the surface. Integrated over the surface, friction and pressure drag from the bed shear stress and the pressure distribution, respectively, make up the total shear stress, τ (Leonardi et al. 2007). The double-averaged Reynolds stresses ($\langle \overline{u'2+} \rangle$, $-\langle \overline{u'v'+} \rangle$, $\langle \overline{v'2+} \rangle$), normalized by U_τ^2 , also show a lack of outer layer similarity (Figure 3C, D and E). Smooth-wall streamwise Reynolds stress ($\langle \overline{u'2+} \rangle$) classically exhibits a peak adjacent to the wall, where viscous forces become appreciable and low-speed longitudinal streaks populate the boundary layer. This is not seen over the patchy and uniform biofilms (Figure 3C), indicating that these biofilms are hydraulically rough (Ligrani and Moffat 1986). Hence, for these surfaces, it would be expected that the roughness of the biofilm is larger than the viscous sublayer and the pressure (form) drag dominates over the viscous stress, destroying the low-speed streaks. The sparse surfaces appear to have a near-wall peak, indicating that these fouled surfaces are not in the fully rough regime (Brzek et al. 2007). For the hydraulically rough biofilms, the broad peak between about $\langle \overline{u'2+} \rangle \cong 3$ and $\langle \overline{u'2+} \rangle \cong 4$ is similar in shape and magnitude to that seen in other studies looking at freshwater and marine biofilms (Schultz and Swain 1999; Walker et al. 2013). The RSS profiles over the patchy and uniform biofilms (PB-1, PB-2 and UB) have the peak shifted away from the wall as compared with the sparse biofilms and the smooth wall, with PB-1 exhibiting a broad plateau region. This upward (away from the wall) shift in the location of the RSS peak indicates a relative increase in the friction due to drag relative to viscous forces.

Figure 3F, G and H presents the double-averaged dispersive stress profiles over each biofilm. The dispersive stresses are the products of the fluctuating components of the time-averaged streamwise and wall-normal velocities, $\langle \sim u \sim u \rangle$, $\langle \sim u \sim v \rangle$, and $\langle \sim v \sim v \rangle$ (Figure 3F, G and H). Dispersive stresses arise from the form-induced wake resulting from roughness topography (Yuan and Piomelli 2014). The

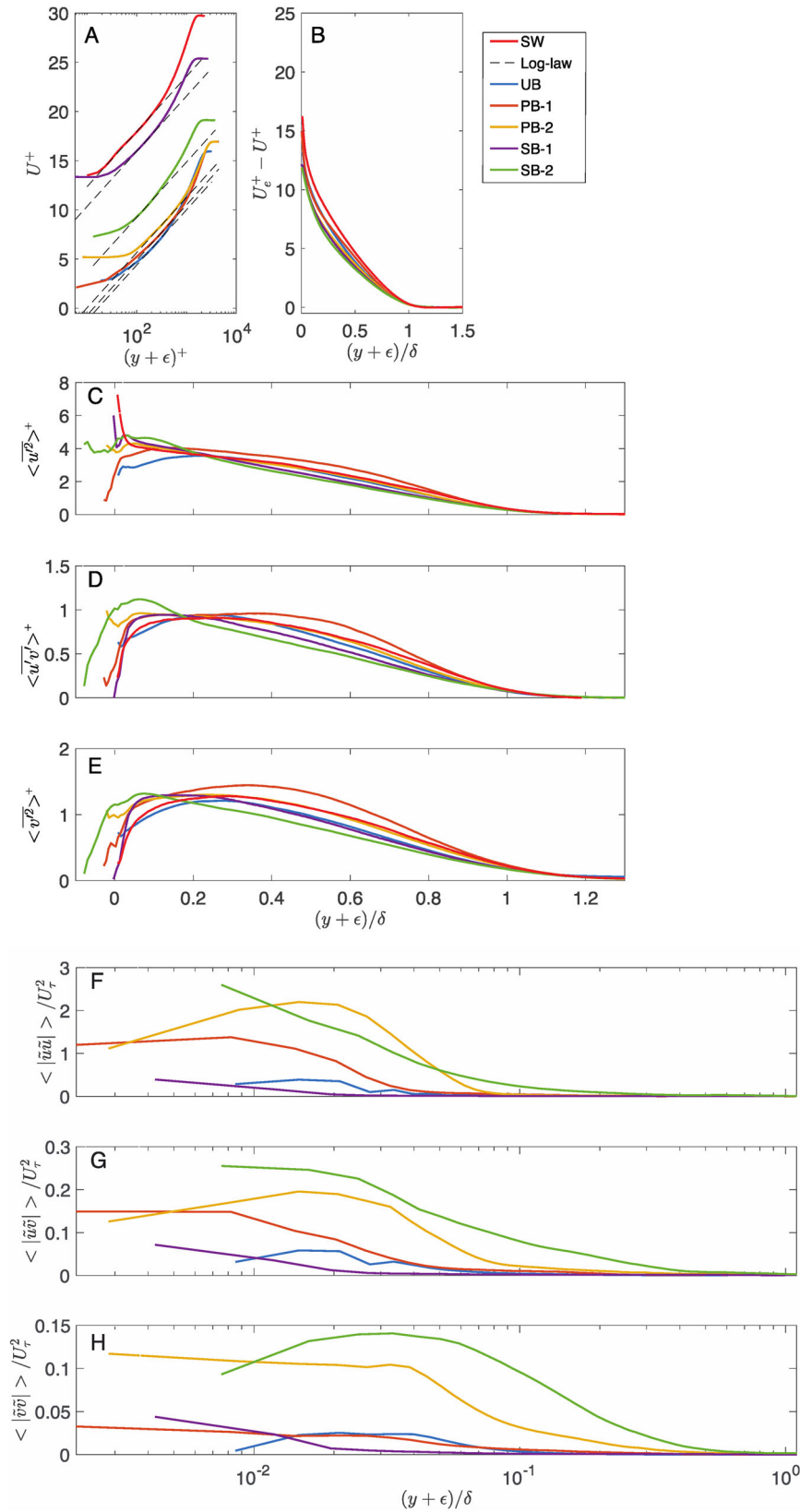


Figure 3. Double-averaged mean streamwise velocity profiles (A & B), Reynolds stress profiles (C, D & E), and dispersive stress profiles (F, G & H) over each biofilm. U is plotted in inner units (A), where U is normalized by U_τ and y is normalized by $\frac{y}{U_\tau}$, and in velocity defect form (B). The double-averaged Reynolds stress and dispersive stress profiles are plotted in inner units. The smooth wall case (red line) is given for comparison for the Reynolds stresses, but is negligible and not shown for the dispersive stresses.

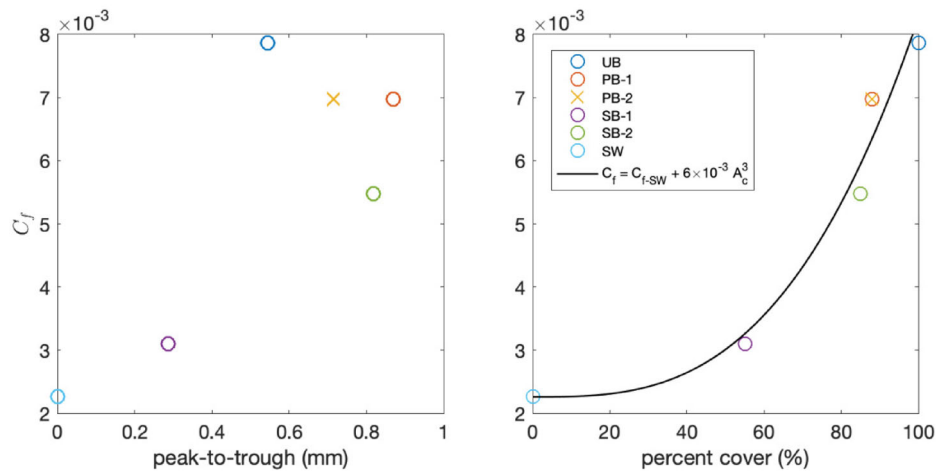


Figure 4. Skin friction (C_f) of the biofilm surfaces, plotted against the peak-to-trough distance of the biofilm surface and the percent cover of the biofilm. The black line shows a power law equation fit to the data, where C_{f-SW} is the smooth wall skin friction value and A_c is the percent cover of the biofilm.

wall-normal and shear dispersive stresses over the biofilms are much lower than the corresponding Reynolds stresses, even below the height of the crest of biofilm roughness elements, further indicating the dominance of turbulent rather than wake momentum transport (Mignot et al. 2009). PB-2 and SB-1 both have elevated dispersive stresses as compared to the other biofilm surfaces, and exhibit elevated dispersive stresses further from the wall, indicating a thickened roughness sublayer. The roughness sublayer is the region of the boundary layer where the roughness results in spatial variability in the time-averaged velocity (Yuan and Piomelli 2014).

The three Reynolds stress profiles do not collapse well in the outer layer, calling into question whether or not outer layer similarity is a valid assumption for biofilms. This may have implications for attempts to upscale skin friction results from laboratory studies to estimate drag penalties on, e.g. ships (Schultz 2007). Other studies, however, have found outer layer similarity for biofilm fouled surfaces (Walker et al. 2013).

The integrated friction velocity (U_τ), determined from the streamwise averaged mean velocity profile, is larger over the biofilms compared with the smooth wall (Table 2). Keeping in mind that the two patchy tests (PB-1 and PB-2) were conducted on the same plate, at the same downstream location but offset spanwise locations, it is interesting to note that they have almost the same integrated U_τ value (0.078 and 0.079 m s^{-1}) despite different local topographies (as evidenced by differing mean and maximum peak-to-trough distances, as presented in Table 1).

The mean velocity profiles were used to calculate roughness effects on the flow (Table 2). The skin-friction coefficient ($C_f = 2 \frac{U_\tau^2}{U_e^2}$) appears to be most

strongly influenced by the percent cover of the biofilm, as opposed to the physical roughness height (measured as the mean peak-to-trough distance) of the biofilm (Figure 4). This could be due to the flapping streamers of the biofilm being most important to extracting momentum from the mean flow, as opposed to the rugosity of the biofilm. One important aspect of biofilm fouling, especially on ship hulls, is the drag penalty, which leads to an increase in fuel usage (Hunsucker et al. 2018). A closer look at the results in Figure 4B reveals an apparent power-law dependency of C_f with respect to the percent cover. The authors propose a simple empirical model that captures such behavior. By taking the increase in drag above the smooth level, i.e. $C_f - C_{f-SW}$, the power-law model can be written as $C_f = C_{f-SW} + mA_c^b$, where A_c is the biofilm percent cover. By fitting this model to the data, the estimation of the constants can be simplified to $m = 6 \times 10^{-3}$ and $b = 3$. Such a model may provide some general guidance to how much drag penalty is added by algal biofilm based on simple hull inspection. However, this relationship may change with different flow speeds (Hartenberger et al. 2020). It is important to keep in mind that the hydrodynamic conditions present in the facility used here diverge from those in real world conditions, especially when considering drag penalty on a ship. The freestream velocity used in these tests was around an order of magnitude lower than what might be seen when a ship is underway (e.g. 7.7 m s^{-1} cruising and 15.4 m s^{-1} maximum speeds for typical mid-size Naval ships (Schultz 2007) and 11.3 m s^{-1} cruising speed for cruise ships (Hunsucker et al. 2014)). The external, unbounded ship boundary layer may behave differently from a bounded flow within a flow tunnel,

especially because the biofilm thickness may be larger relative to the boundary layer thickness in a flow tunnel. The external boundary layer on a ship hull, for example, can exceed 1 m in thickness for long ships, and thickens along the length of the ship; additionally, wake dynamics can occur where there is flow separation from the hull (Schultz and Swain 2000). In addition to these caveats, it must be noted that, with only 5 points, the power law fit to the C_f may not be very robust.

The downward shift noted in the biofilm velocity profiles (Figure 3A) is a result of momentum extracted from the flow by the biofilm. This is quantified by the roughness function, ΔU^+ (Table 2). The physical analogy for the roughness function, the effective sand grain height, provides a means of relating the effects of different types of roughness to the drag produced by uniform, closely packed sand grains on pipe walls (Nikuradse 1933). The effective sand grain height is a function of ΔU^+ ($k_s^+ = \exp(\kappa(\Delta U^+ + 3.5))$), and also appears dependent on the biofilm percent cover more than the physical roughness height (Table 2). As seen over a uniform biofilm (Murphy et al. 2018), the patchy biofilms result in a larger k_s value than the physical height of the biofilm surface roughness. However, the calculation of k_s^+ is only strictly valid in the fully rough regime, so values for the sparse biofilms should be interpreted with some caution (Flack et al. 2012).

The local value of U_τ was calculated for every fifth vertical velocity profile in each frame, using the CSS method, and are shown in Figure 5 (normalized by U_e). Also shown is the local topography of the biofilm. The local values of U_τ appear fairly homogenous (Figure 5B, C and E). Interestingly, the lower values of U_τ seems to correspond with locations of low or absent topography (regions of low relative local change in the height of the surface of the biofilm). Additionally, the local peaks and valleys of U_τ seem to relate to sharp changes of the local biofilm thickness, i.e. high gradient of the topography. One important point when considering these data is that the calculations of the local U_τ assumes local equilibrium in the flow, and that the local log-law represents the local conditions. Especially for the patchy roughness, which may not exhibit outer layer similarity, these assumptions may not hold. However, because the CSS method also uses the local RSS profile to calculate the local U_τ , this might be less problematic than when using a method that solely fits U to the log-law, such as the modified Clauser chart.

The dispersive stress over the biofilms is highly variable in the streamwise direction. Over a uniform biofilm, there are localized regions of elevated dispersive stress right at the biofilm surface (Murphy et al. 2018). Over the patchy and sparse biofilms, there is greater heterogeneity in dispersive stresses, with PB-1 and PB-2 exhibiting rather dissimilar patterns despite being located on the same plate (Figure 6A and B). In addition to near-bed hotspots, SB-2 and PB-2 have areas of enhanced dispersive stress elevated off the bed, at the height of the crest of the biofilm roughness elements (Figure 6B and C). Dispersive stresses are important to mass transport, especially in canopy flows (Poggi et al. 2004), so the layer of increased dispersive stress over the patchy and sparse biofilms may contribute to local hotspots of nutrient transport related to the canopy flow over the more rugose biofilms. Spatially explicit plots of tke production ($\overline{P} = -\overline{u'v'} \frac{\partial U}{\partial y}$, here normalized as $\overline{P}^+ = \overline{P} \frac{U_e^3}{\rho}$) over a patchy and a sparse biofilm reveal that tke production is highly localized (Figure 6D, E and F). \overline{P}^+ appears to be enhanced downstream of some of the protruding biofilm structures, and in the 6B-2 panel (Figure 6F) \overline{P}^+ is only elevated over the more rough areas of biofilm, with little tke production in the low relief area of the biofilm in the middle of the frame.

Coherent structures

Coherent structures in turbulent boundary layer flows are key to momentum and mass transport to and from the bed. Quadrant analysis is a conditional averaging technique used to determine the strength of turbulent sweeps (where high momentum flow in the outer layer travels toward the bed; Q4) and ejections (where low momentum fluid from the near-bed region is ejected higher up into the boundary layer; Q2) (Reidenbach et al. 2007; Wallace 2016). Here the quadrant-hole technique (Lu and Willmarth 1973) was used to determine the relative contributions of strong ($|u'v'| > H\sigma_u\sigma_v$; where $H = 4$ and σ_{u_i} is the standard deviation of u_i at a given location) instantaneous vertical turbulent events to the Reynolds shear stress. In other words, what is presented here is the time-average of the instantaneous $u'v'$ events (that exceed the given threshold) that fall within the specified quadrant. This also shows the vertical stratification of strong instantaneous events in the boundary layer, and the streamwise variability of these events over the different biofilms (Figure 7). Q2 events are strongest in the outer layer, while Q4 events dominate at the bed, as is typical over rigid roughness and canopy flows (Raupach 1981; Yue et al. 2007). All of the

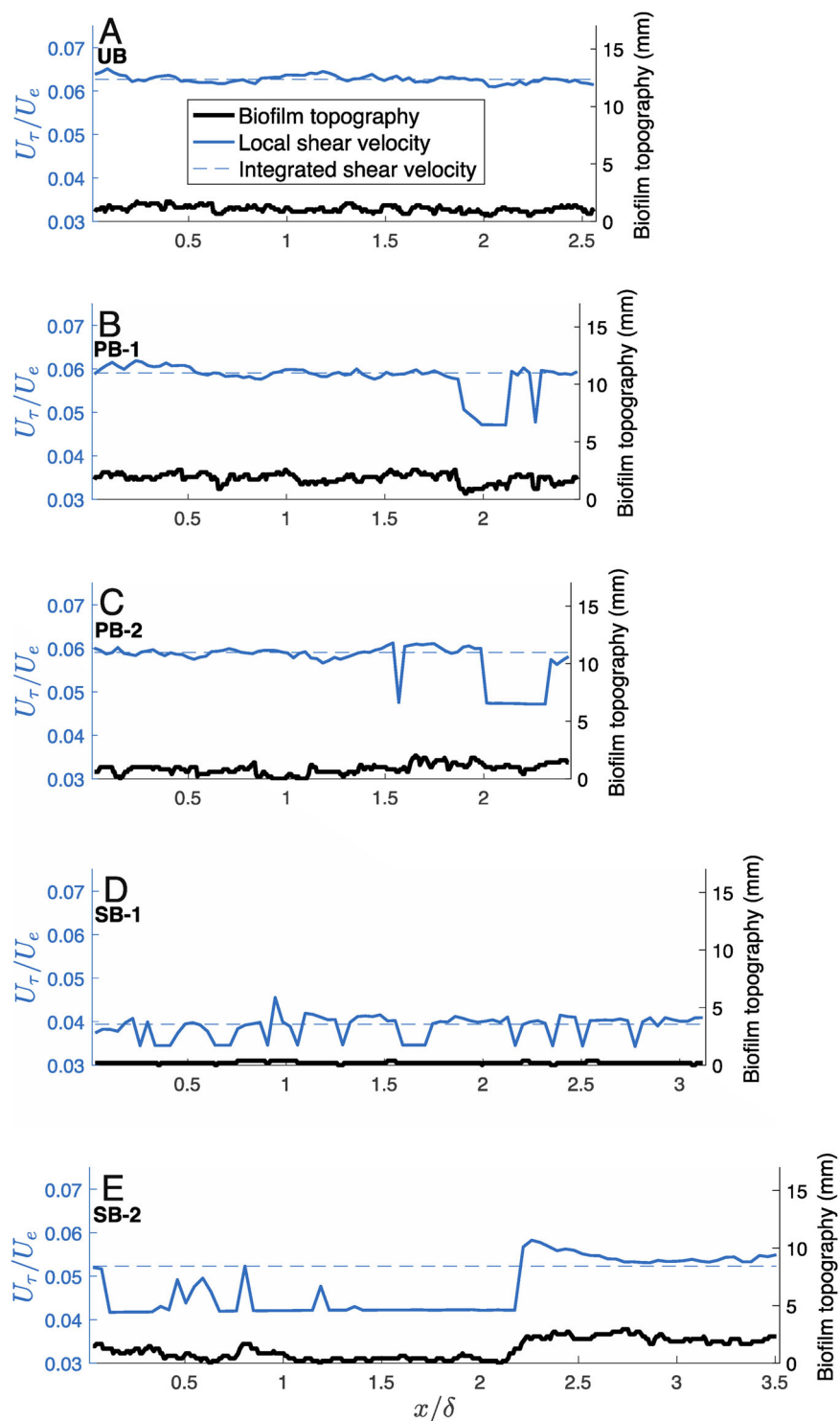


Figure 5. Local shear velocity (U_τ) normalized by the freestream velocity (U_e) (solid blue line), plotted with the biofilm topography in each frame (solid black line). The integrated U_τ is given for comparison (dashed blue line).

biofilms, aside from SB-1, which, as discussed previously, has very low biofilm roughness and coverage, have similar magnitudes of strong turbulent ejections near the bed. The magnitude of strong turbulent sweeps, however, is dependent on the biofilm surface, with the patchy biofilms both having large, sharp peaks (Supplemental Figure 1), indicating that for the patchy

biofilm, entrainment of high velocity flow down toward the bed is especially important. This may mean that there is stronger vortex shedding from the patchy biofilms, because Q4 events over canopies are a result of prograde (rotating with the direction of the mean shear) vortices being shed off of the vegetation at the canopy top. This likely results in increased transport of scalar

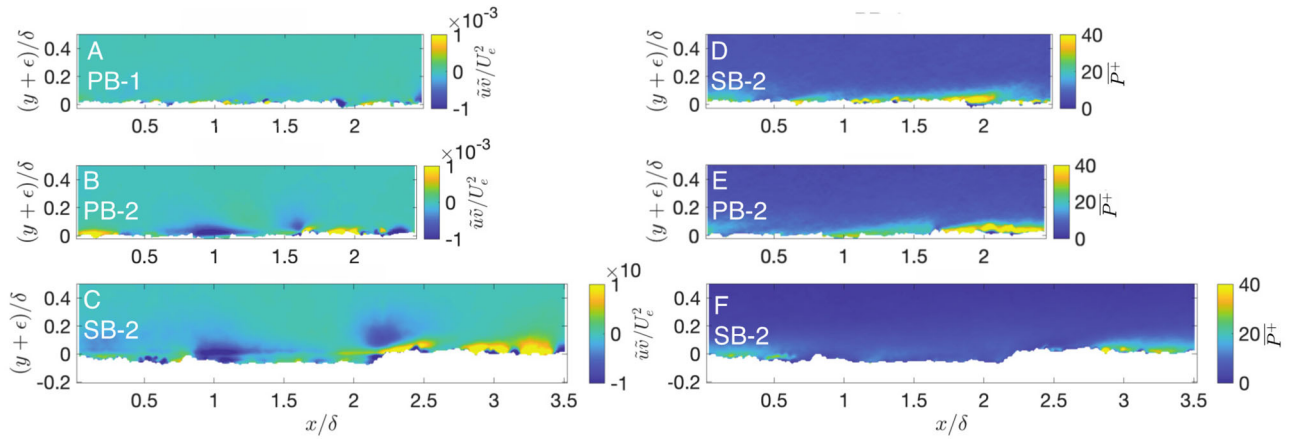


Figure 6. Dispersive stresses (panels A, B, C) and turbulent kinetic energy production ($\overline{P^+}$) (panels D, E, F) over three of the tested biofilms. (A & D) Patchy 1; (B & E) Patchy 2; (C & F) Sparse 2. For $\overline{P^+}$, Each local vertical profile of U was smoothed with a smoothing spline before finding $\frac{\partial U}{\partial y}$ in P .

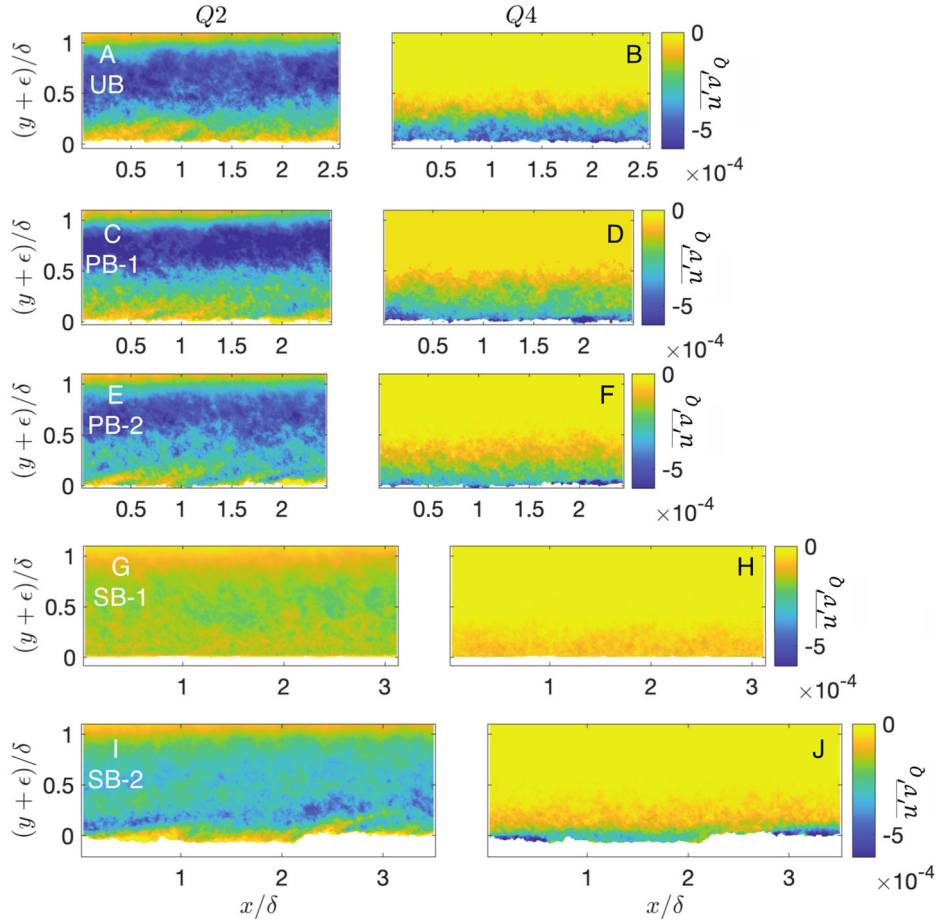


Figure 7. Quadrant-hole analysis with $H=4$. (A & B) Uniform biofilm; (C & D) Patchy 1 biofilm; (E & F) Patchy 2 biofilm; (G & H) Sparse 1 biofilm; (I & J) Sparse 2 biofilm. The results show the contribution of $u'v'$ values that exceed the threshold value in the given quadrant; $\overline{u'v'}_{Q2}$ and $\overline{u'v'}_{Q4}$ are normalized by U_e^2 .

quantities, such as free swimming larvae or sediment, to the biofilm surface (Hendriks et al. 2006).

The swirling strength, λ_{ci} , is a measure of rotational flow similar to the vorticity, ω , however, the vorticity includes shear whereas the swirling strength is a measure

solely of the rotational component of the fluid motion (Zhou et al. 1999). The swirling strength is the imaginary part of the complex eigenvalue of the local instantaneous velocity gradient. Here, the instantaneous λ_{ci} is used along with the instantaneous velocity field to identify

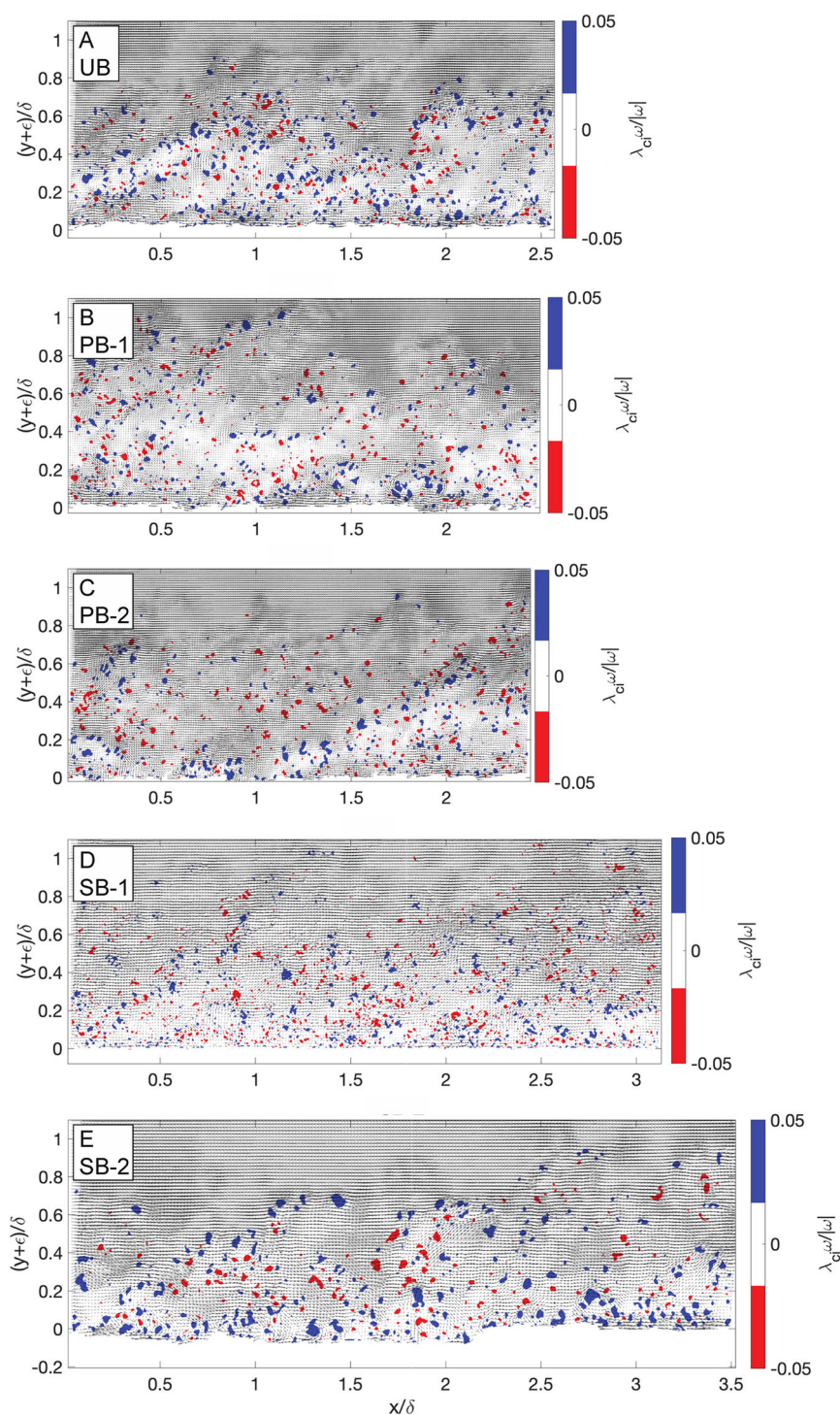


Figure 8. Galilean decomposition of an instantaneous flow field over each biofilm, with $0.7 U_e$ removed. The Galilean decompositions are plotted over λ_{Gal} , the swirling strength, to highlight locations of rotational flow. Location of prograde rotation (rotating in the direction of the flow) are shaded in blue, and locations of retrograde rotation (rotating in the direction opposite the mean flow) are red.

vortices and coherent structures within the flow. Galilean decomposition was used to investigate the small-scale eddies in the flow. This technique removes the convective velocity from the instantaneous velocity field so that $u_c = u - U_c$, where U_c is the Galilean convection velocity (Adrian et al. 2000; Volino et al. 2007) as a

percentage of the freestream velocity. The local instantaneous vorticity is used to give a sign (direction of rotation) to the swirling strength so that prograde (rotating in the direction of the mean shear) and retrograde (rotating the opposite direction of the mean shear) vortices can be distinguished (Wu and Christensen 2006).

Galilean-decomposed instantaneous velocity fields over the biofilms, with a convective velocity of $0.7U_e$ removed, are shown in [Figure 8](#). The Galilean decompositions are plotted over λ_{ci} , the swirling strength, to highlight locations of rotational flow. Because most of the freestream velocity is removed from each velocity vector, this highlights lower-speed vortices near the bed, which occur more often in packets. These vortices entrain fluid, moving high-momentum fluid downwards to the bed and low-momentum fluid upwards. As in other turbulent boundary layer flows, this mechanism of momentum transport appears important in biofilm-bounded flow (Volino et al. 2009; Wu and Christensen 2010). The uniform and patchy biofilms appear to have prograde vortex streets being shed from the wall ([Figure 8A, B and C](#)). SB-1 has noticeably smaller locations of rotating flow ([Figure 8D](#)), and the instantaneous flow appears more disorganized than over the other biofilms. The Galilean decomposed velocity fields over the patchy biofilms may show larger scale groups of vortices extending nearly the entire height of the boundary layer ([Figure 8B and C](#)), as seems to be more common over 2D roughness than 3D roughness. This may be a result of the larger scale patchiness of the biofilm, where large patches of biofilm free surface may allow reattachment of the flow before it encounters subsequent biofilm covered areas (Volino et al. 2011). While these results are interesting, and suggestive of the effects of biofilm topography on larger-scale attached eddies, the constraints of the experimental system, especially considering the relative height of the biofilm roughness compared with the limited height of the boundary layer in the flow tunnel, and the potential for wall effects, make it difficult to extrapolate these results to external boundary layers such as in flow over a ship (Volino et al. 2009).

Conclusions

The drag coefficient of the biofilm appears to correlate most strongly with percent cover of the biofilm, rather than peak-to-trough distance, which means that the uniform biofilm has the greatest increase in surface drag despite not having the largest roughness elements. This may be due to the cumulative effects of a larger area of compliant surface, and a larger number of flapping streamers removing momentum from the flow. This suggests that a simple measure of percent biofilm cover could be the most important parameter to track when determining the impact of soft fouling on ship performance. However, notable

differences between the experimental flow tunnel employed here, with an internal boundary layer at lower free stream velocities compared to an external boundary layer as would be seen over a ship hull, make further investigation of the applicability of our results to real world scenarios important.

Non-uniform biofilms enhance vertical momentum transport in the boundary layer, at least in part due to setting up local plane mixing layers where the velocity profiles are S-shaped. Given the increase in energy of the vortices over the patchy biofilms and the exposed bed under patchy biofilms, non-uniform biofilms may in fact increase vertical fluxes of mass and momentum to the underlying substrate. The high energy loss of flow over biofilms, possibly due to the flapping streamers, combined with the low relief of the biofilms, means that vertical transport can be greatly increased, albeit in a spatially heterogeneous manner. Because biofilms are typically the first biofouling community to colonize a surface, and facilitate the settlement and development of further biofouling organisms, the implications of this are worth considering in the context of biofilm community development.

As a biofilm matures and get too thick for deeper cells to access nutrients, senescence and sloughing due to high shear results in biofilm patchiness and altered local hydrodynamics, potentially resulting in more localized sloughing as well as enhanced turbulent transport of metabolites to the bed, as evidenced by the spike in turbulent sweep strength over patchy biofilms ([Supplemental Figure 1](#)). This interaction between biofilm morphology and hydrodynamics therefore may enhance the fitness of the biofilm community. Additionally, local hydrodynamics may be important to the later development of the fouling community. The increase in turbulent sweeps and ejections, especially over the patchy biofilms ([Figure 7 and Supplemental Figure 1](#)) affect where larvae settle on a biofilm fouled surface and whether the larvae are able to stick to the surface (Koehl 2007; Hata et al. 2017). In addition, the pockets of lower shear stress and lower momentum flow that are especially evident in the non-uniform biofilm may provide suitable location for the settlement of larvae.

Acknowledgements

The authors are grateful for technical support provided by the USNA Technical Support Division and the USNA Hydromechanics Lab. The authors also wish to acknowledge the detailed and constructive criticism of two anonymous reviewers, which significantly improved the manuscript.

Disclosure statement

No potential conflict of interest was reported by the authors.

Funding

This work was supported by the U.S. Office of Naval Research Grant #N0001417-WX-00846; U.S. Office of Naval Research Grant # N00014-15-1-2560; U.S. National Science Foundation Graduate Research Internship Program Fellowship #2014162109; U.S. National Science Foundation Graduate Research Fellowship Program #DDGE-1315231.

ORCID

Elizabeth A. K. Murphy  <http://orcid.org/0000-0003-3316-7328>

Julio M. Barros  <http://orcid.org/0000-0003-4283-2262>

Michael P. Schultz  <http://orcid.org/0000-0003-1997-801X>

Matthew A. Reidenbach  <http://orcid.org/0000-0002-5592-920X>

Data availability statement

The instantaneous vector fields used to analyze flow over the patchy biofilm plates are freely available on Zenodo at <https://doi.org/10.5281/zenodo.5644626>

References

- Adrian RJ, Christensen KT, Liu Z-C. 2000. Analysis and interpretation of instantaneous turbulent velocity fields. *Exp Fluids*. 29:275–290. doi:10.1007/s003489900087
- Andrewartha J, Perkins K, Sargison J, Osborn J, Walker G, Henderson A, Hallegraef G. 2010. Drag force and surface roughness measurements on freshwater biofouled surfaces. *Biofouling*. 26:487–496. doi:10.1080/08927014.2010.482208.
- Antonia RA, Luxton RE. 1971. The response of a turbulent boundary layer to a step change in surface roughness Part 1. Smooth to rough. *J Fluid Mech*. 48:721–761. doi:10.1017/S0022112071001824
- Battin TJ, Kaplan LA, Denis Newbold J, Hansen CME. 2003. Contributions of microbial biofilms to ecosystem processes in stream mesocosms. *Nature*. 426:439–442. doi:10.1038/nature02152.
- de Beer D, Kühl M. 2001. Interfacial microbial mats and biofilms. In: Boudreau BP, Jørgensen BB, editors. *The benthic boundary layer*. New York, NY: Oxford University Press; p. 374–394.
- Brzek BG, Cal RB, Johansson G, Castillo L. 2007. Transitionally rough zero pressure gradient turbulent boundary layers. *Exp Fluids*. 44:115–124. doi:10.1007/s00348-007-0380-5
- Celler K, Hödl I, Simone A, Battin TJ, Picioreanu C. 2014. A mass-spring model unveils the morphogenesis of phototrophic Diatoma biofilms. *Sci Rep*. 4:3649. doi:10.1038/srep03649.
- Decho AW. 2000. Microbial biofilms in intertidal systems: an overview. *Cont Shelf Res*. 20:1257–1273. doi:10.1016/S0278-4343(00)00022-4
- Depetris A, Tagliavini G, Peter H, Kühl M, Holzner M, Battin TJ. 2022. Biophysical properties at patch scale shape the metabolism of biofilm landscapes. *NPJ Biofilms Microbiomes*. 8:5. doi:10.1038/s41522-022-00269-0.
- Dobretsov S, Rittschof D. 2020. Love at first taste: induction of larval settlement by marine microbes. *Int J Mol Sci*. 21:731. doi:10.3390/ijms21030731
- Eckman JE. 1990. A model of passive settlement by planktonic larvae onto bottoms of differing roughness. *Limnol Oceanogr*. 35:887–901. doi:10.4319/lo.1990.35.4.0887
- Flack KA, Schultz MP. 2014. Roughness effects on wall-bounded turbulent flows. *Phys Fluids*. 26:101305. doi:10.1063/1.4896280
- Flack KA, Schultz MP, Connelly JS. 2007. Examination of a critical roughness height for outer layer similarity. *Phys Fluids*. 19:095104. doi:10.1063/1.2757708
- Flack KA, Schultz MP, Rose WB. 2012. The onset of roughness effects in the transitionally rough regime. *Int J Heat Fluid Flow*. 35:160–167. doi:10.1016/j.ijheatfluidflow.2012.02.003
- Florens E, Eiff O, Moulin F. 2013. Defining the roughness sublayer and its turbulence statistics. *Exp Fluids*. 54:1500. doi:10.1007/s00348-013-1500-z
- Fuchs HL, Neubert MG, Mullineaux LS. 2007. Effects of turbulence-mediated larval behavior on larval supply and settlement in tidal currents. *Limnol Oceanogr*. 52:1156–1165. doi:10.4319/lo.2007.52.3.1156
- Graba M, Sauvage S, Majdi N, Mialet B, Moulin FY, Urrea G, Buffan-Dubau E, Tackx M, Sabater S, Sanchez-Pérez J-M. 2014. Modelling epilithic biofilms combining hydrodynamics, invertebrate grazing and algal traits. *Freshw Biol*. 59:1213–1228. doi:10.1111/fwb.12341
- Graba M, Sauvage S, Moulin FY, Urrea G, Sabater S, Sanchez-Pérez JM. 2013. Interaction between local hydrodynamics and algal community in epilithic biofilm. *Water Res*. 47:2153–2163. doi:10.1016/j.watres.2013.01.011.
- Grass AJ. 1971. Structural features of turbulent flow over smooth and rough boundaries. *J Fluid Mech*. 50:233–255. doi:10.1017/S0022112071002556
- Hadfield M, Paul V. 2001. Natural Chemical Cues for Settlement and Metamorphosis of Marine-Invertebrate Larvae. In: McClintock J, Baker B, editors. *Marine chemical ecology*. Vol. 20015660: Boca Raton: CRC Press; p. 431–461. doi:10.1201/9781420036602.ch13
- Hansen JCR, Reidenbach MA. 2012. Wave and tidally driven flows in eelgrass beds and their effect on sediment suspension. *Mar Ecol Prog Ser*. 448:271–287. doi:10.3354/meps09225
- Hartenberger JD, Callison EG, Gose JW, Perlin M, Ceccio SL. 2020. Drag production mechanisms of filamentous biofilms. *Biofouling*. 36:736–752. doi:10.1080/08927014.2020.1806250.
- Hata T, Madin JS, Cumbo VR, Denny M, Figueiredo J, Harii S, Thomas CJ, Baird AH. 2017. Coral larvae are poor swimmers and require fine-scale reef structure to settle. *Sci Rep*. 7:2249. doi:10.1038/s41598-017-02402-y

- Hendriks IE, van Duren LA, Herman PM. 2006. Turbulence levels in a flume compared to the field: implications for larval settlement studies. *J Sea Res.* 55: 15–29. doi:10.1016/j.seares.2005.09.005
- Hunsucker JT, Hunsucker KZ, Gardner H, Swain G. 2016. Influence of hydrodynamic stress on the frictional drag of biofouling communities. *Biofouling.* 32:1209–1221. doi:10.1080/08927014.2016.1242724.
- Hunsucker KZ, Koka A, Lund G, Swain G. 2014. Diatom community structure on in-service cruise ship hulls. *Biofouling.* 30:1133–1140. doi:10.1080/08927014.2014.974576.
- Hunsucker KZ, Vora GJ, Hunsucker JT, Gardner H, Leary DH, Kim S, Lin B, Swain G. 2018. Biofilm community structure and the associated drag penalties of a groomed fouling release ship hull coating. *Biofouling.* 34:162–172. doi:10.1080/08927014.2017.1417395.
- Kevin K, Monty JP, Bai HL, Pathikonda G, Nugroho B, Barros JM, Christensen KT, Hutchins N. 2017. Cross-stream stereoscopic particle image velocimetry of a modified turbulent boundary layer over directional surface pattern. *J Fluid Mech.* 813:412–435. doi:10.1017/jfm.2016.879
- Koehl MAR. 2006. The fluid mechanics of arthropod sniffing in turbulent odor plumes. *Chem Senses.* 31:93–105. doi:10.1093/chemse/bjj009.
- Koehl MRA. 2007. Mini review: hydrodynamics of larval settlement into fouling communities. *Biofouling.* 23: 357–368. doi:10.1080/08927010701492250.
- Koehl MAR, Perotti E, Sicho D, Hata T, Hadfield MG. 2022. Effects of currents, waves, and biofilms on motion and surface contacts by tubeworm larvae swimming above or below surfaces. *Mar Ecol Prog Ser.* 686: 107–126. doi:10.3354/meps14001
- Krogstad PÅ, Antonia RA. 1999. Surface roughness effects in turbulent boundary layers. *Exp Fluids.* 27:450–460. doi:10.1007/s003480050370
- Leonardi S, Orlandi P, Antonia RA. 2007. Properties of d- and k-type roughness in a turbulent channel flow. *Phys Fluids.* 19:125101. doi:10.1063/1.2821908
- Ligrani PM, Moffat RJ. 1986. Structure of transitionally rough and fully rough turbulent boundary layers. *J Fluid Mech.* 162:69–98. doi:10.1017/S0022112086001933
- Lu SS, Willmarth WW. 1973. Measurements of the structure of the Reynolds stress in a turbulent boundary layer. *J Fluid Mech.* 60:481–511. doi:10.1017/S0022112073000315
- Martino R, Paterson A, Piva M. 2012. Double-average mean flow and local turbulence intensity profiles from PIV measurements for an open channel flow with rigid vegetation. *Environ Fluid Mech.* 12:45–62. doi:10.1007/s10652-011-9221-4
- Mignot E, Barthelemy E, Hurther D. 2009. Double-averaging analysis and local flow characterization of near-bed turbulence in gravel-bed channel flows. *J Fluid Mech.* 618:279–303. doi:10.1017/S0022112008004643
- Mignot E, Hurther D, Barthelemy E. 2009. On the structure of shear stress and turbulent kinetic energy flux across the roughness layer of a gravel-bed channel flow. *J Fluid Mech.* 638:423–452. doi:10.1017/S0022112009990772
- Murphy EAK, Barros JM, Schultz MP, Flack KA, Steppe CN, Reidenbach MA. 2018. Roughness effects of diatomaceous slime fouling on turbulent boundary layer hydrodynamics. *Biofouling.* 34:1–12. doi:10.1080/08927014.2018.1517867
- Nepf HM, Vivoni ER. 2000. Flow structure in depth-limited, vegetated flow. *J Geophys Res.* 105:28547–28557. doi:10.1029/2000JC900145
- Nikora V, McEwan I, McLean S, Coleman S, Pokrajac D, Walters R. 2007. Double-averaging concept for rough-bed open-channel and overland flows: theoretical background. *J Hydraul Eng.* 133:873–883. doi:10.1061/(ASCE)0733-9429(2007)133:8(873)
- Nikuradse J. 1933. Laws of flow in rough pipes. NACA Technical Memorandum 1292.
- Poggi D, Katul GG, Albertson JD. 2004. A note on the contribution of dispersive fluxes to momentum transfer within canopies. *Bound-Layer Meteorol.* 111:615–621. doi:10.1023/B:BOUN.0000016563.76874.47
- Pokrajac D, Campbell LJ, Nikora V, Manes C, McEwan I. 2007. Quadrant analysis of persistent spatial velocity perturbations over square-bar roughness. *Exp Fluids.* 42: 413–423. doi:10.1007/s00348-006-0248-0
- Raupach MR. 1981. Conditional statistics of Reynolds stress in rough-wall and smooth-wall turbulent boundary layers. *J Fluid Mech.* 108:363–382. doi:10.1017/S0022112081002164
- Raupach MR, Finnigan JJ, Brunei Y. 1996. Coherent eddies and turbulence in vegetation canopies: the mixing-layer analogy. *Boundary-Layer Meteorol.* 78:351–382. doi:10.1007/978-94-017-0944-6_15
- Raupach MR, Shaw RH. 1982. Averaging procedures for flow within vegetation canopies. *Boundary-Layer Meteorol.* 22:79–90. doi:10.1007/BF00128057
- Reidenbach MA, Koseff JR, Monismith SG. 2007. Laboratory experiments of fine-scale mixing and mass transport within a coral canopy. *Phys Fluids.* 19:075107. doi:10.1063/1.2752189
- Reidenbach MA, Limm M, Hondzo M, Stacey MT. 2010. Effects of bed roughness on boundary layer mixing and mass flux across the sediment-water interface. *Water Resour Res.* 46:W07530. doi:10.1029/2009WR008248
- Schultz MP. 2000. Turbulent boundary layers on surfaces covered with filamentous algae. *J Fluids Eng.* 122: 357–363. doi:10.1115/1.483265
- Schultz MP. 2007. Effects of coating roughness and biofouling on ship resistance and powering. *Biofouling.* 23: 331–341. doi:10.1080/08927010701461974.
- Schultz MP, Bendick JA, Holm ER, Hertel WM. 2011. Economic impact of biofouling on a naval surface ship. *Biofouling.* 27:87–98. doi:10.1080/08927014.2010.542809.
- Schultz MP, Finlay JA, Callow ME, Callow JA. 2003. Three models to relate detachment of low form fouling at laboratory and ship scale. *Biofouling.* 19:17–26. doi:10.1080/0892701031000089516
- Schultz MP, Swain GW. 1999. The effect of biofilms on turbulent boundary layers. *J Fluids Eng.* 121:44–51. doi:10.1115/1.2822009
- Schultz MP, Swain GW. 2000. The influence of biofilms on skin friction drag. *Biofouling.* 15:129–139. doi:10.1080/08927010009386304.
- Schultz MP, Walker JM, Steppe CN, Flack KA. 2015. Impact of diatomaceous biofilms on the frictional drag

- of fouling-release coatings. *Biofouling*. 31:759–773. doi:10.1080/08927014.2015.1108407.
- Snyder WH, Castro IP. 2002. The critical Reynolds number for rough-wall boundary layers. *J Wind Eng Ind Aerodyn*. 90:41–54. doi:10.1016/S0167-6105(01)00114-3
- Stocking JB, Rippe JP, Reidenbach MA. 2016. Structure and dynamics of turbulent boundary layer flow over healthy and algae-covered corals. *Coral Reefs*. 35:1047–1059. doi:10.1007/s00338-016-1446-8
- Stoodley P, Lewandowski Z, Boyle JD, Lappin-Scott HM. 1998. Oscillation characteristics of biofilm streamers in turbulent flowing water as related to drag and pressure drop. *Biotechnol Bioeng*. 57:536–544. doi:10.1002/(SICI)1097-0290(19980305)57:5 < 536::AID-BIT5 > 3.0.CO;2-H
- Stoodley P, Lewandowski Z, Boyle JD, Lappin-Scott HM. 1999. Structural deformation of bacterial biofilms caused by short-term fluctuations in fluid shear: an in situ investigation of biofilm rheology. *Biotechnol Bioeng*. 65:11.
- Swain GW. 2010. The importance of ship hull coatings and maintenance as drivers for environmental sustainability. *Proceedings of Ship Design and Operation for Environmental Sustainability; Mar 2010; London: Royal Institute of Naval Architects*. doi:10.3940/rina.es.2010.17
- Taherzadeh D, Picioreanu C, Horn H. 2012. Mass transfer enhancement in moving biofilm structures. *Biophys J*. 102:1483–1492. doi:10.1016/j.bpj.2012.02.033.
- Telgmann U, Horn H, Morgenroth E. 2004. Influence of growth history on sloughing and erosion from biofilms. *Water Res*. 38:3671–3684. doi:10.1016/j.watres.2004.05.020.
- Van Mooy BAS, Hmelo LR, Fredricks HF, Ossolinski JE, Pedler BE, Bogorff DJ, Smith PJS. 2014. Quantitative exploration of the contribution of settlement, growth, dispersal and grazing to the accumulation of natural marine biofilms on antifouling and fouling-release coatings. *Biofouling*. 30:223–236. doi:10.1080/08927014.2013.861422.
- Volino RJ, Schultz MP. 2018. Determination of wall shear stress from mean velocity and Reynolds shear stress profiles. *Phys Rev Fluids*. 3:034606.
- Volino RJ, Schultz MP, Flack KA. 2007. Turbulence structure in rough- and smooth-wall boundary layers. *J Fluid Mech*. 592:263–293. doi:10.1017/S0022112007008518
- Volino RJ, Schultz MP, Flack KA. 2009. Turbulence structure in a boundary layer with two-dimensional roughness. *J Fluid Mech*. 635:75–101. doi:10.1017/S0022112009007617
- Volino RJ, Schultz MP, Flack KA. 2011. Turbulence structure in boundary layers over periodic two- and three-dimensional roughness. *J Fluid Mech*. 676:172–190. doi:10.1017/S0022112011000383
- Walker JM, Flack KA, Lust EE, Schultz MP, Luznik L. 2014. Experimental and numerical studies of blade roughness and fouling on marine current turbine performance. *Renew Energy*. 66:257–267. doi:10.1016/j.renene.2013.12.012
- Walker JM, Sargison JE, Henderson AD. 2013. Turbulent boundary-layer structure of flows over freshwater biofilms. *Exp Fluids*. 54:1628. doi:10.1007/s00348-013-1628-x
- Wallace JM. 2016. Quadrant analysis in turbulence research: history and evolution. *Annu Rev Fluid Mech*. 48:131–158. doi:10.1146/annurev-fluid-122414-034550
- Womack KM, Meneveau C, Schultz MP. 2019. Comprehensive shear stress analysis of turbulent boundary layer profiles. *J Fluid Mech*. 879:360–389. doi:10.1017/jfm.2019.673
- Womack KM, Volino RJ, Meneveau C, Schultz MP. 2022. Turbulent boundary layer flow over regularly and irregularly arranged truncated cone surfaces. *J Fluid Mech*. 933:A38. doi:10.1017/jfm.2021.946
- Wu Y, Christensen KT. 2006. Population trends of spanwise vortices in wall turbulence. *J Fluid Mech*. 568:55–76. doi:10.1017/S002211200600259X
- Wu Y, Christensen KT. 2010. Spatial structure of a turbulent boundary layer with irregular surface roughness. *J Fluid Mech*. 655:380–418. doi:10.1017/S0022112010000960
- Yuan J, Piomelli U. 2014. Roughness effects on the Reynolds stress budgets in near-wall turbulence. *J Fluid Mech*. 760:R1. doi:10.1017/jfm.2014.608
- Yue W, Meneveau C, Parlange MB, Zhu W, Van Hout R, Katz J. 2007. A comparative quadrant analysis of turbulence in a plant canopy. *Water Resour Res*. 43:W05422.
- Zargiel KA, Coogan JS, Swain GW. 2011. Diatom community structure on commercially available ship hull coatings. *Biofouling*. 27:955–965. doi:10.1080/08927014.2011.618268.
- Zargiel KA, Swain GW. 2014. Static vs dynamic settlement and adhesion of diatoms to ship hull coatings. *Biofouling*. 30:115–129. doi:10.1080/08927014.2013.847927.
- Zhou J, Adrian RJ, Balachandar S, Kendall TM. 1999. Mechanisms for generating coherent packets of hairpin vortices in channel flow. *J Fluid Mech*. 387:353–396. doi:10.1017/S002211209900467X